

1 Ion Bernstein instability
2 in the terrestrial magnetosphere:
3 Linear dispersion theory

S. Peter Gary, Kaijun Liu, and Dan Winske

4 Los Alamos National Laboratory, Los Alamos, New Mexico

Richard E. Denton

5 Dartmouth College, Hanover, New Hampshire

S. Peter Gary, Kaijun Liu, and Dan Winske, Los Alamos National Laboratory, Los Alamos,
NM 87545. (e-mail: pgary@lanl.gov, kaijun@lanl.gov, winske@lanl.gov)

Richard E. Denton, Dartmouth College, Hanover, NH. (e-mail:
richard.e.denton@dartmouth.edu)

6 **Abstract.** Linear kinetic dispersion theory for electromagnetic fluctua-
7 tions in a homogeneous, magnetized, collisionless plasma is used to study the
8 properties of an ion Bernstein mode instability driven by a proton velocity
9 distribution $f_p(\mathbf{v})$ such that $\partial f_p(v_\perp)/\partial v_\perp > 0$ where \perp denotes directions
10 perpendicular to the background magnetic field \mathbf{B}_o . Here $f_p(\mathbf{v}) = f_1(v) -$
11 $f_2(v)$ where f_1 and f_2 are Maxwellian velocity distributions with slightly dif-
12 ferent densities and temperatures; plasma parameters are taken from mag-
13 netospheric observations. Then the growth rate of this instability has rela-
14 tive maxima at the fundamental and harmonics of $\omega_r \simeq \Omega_p$, the proton
15 cyclotron frequency, wavevector \mathbf{k} at $0 < k_\parallel \ll k_\perp$ where \parallel and \perp de-
16 note the directions parallel and perpendicular to \mathbf{B}_o , and wavelengths of the
17 order of or smaller than the proton gyroradius. The maximum instability growth
18 rate is a monotonically decreasing function of the electron-to-proton tem-
19 perature ratio, but has its largest value at an intermediate value of the pro-
20 ton β (~ 0.5 for the parameters considered here).

1. Introduction

21 The perpetual restlessness of the magnetosphere manifests itself as a progression of non-
 22 thermal species velocity distributions, the microinstabilities which arise from the various
 23 forms of free energy, and the consequent enhanced field fluctuations. A striking illus-
 24 tration of the various unstable proton velocity distributions which may develop during a
 25 geomagnetic storm has been obtained from the RAM magnetospheric model [*Jordanova*
 26 *et al.*, 1997]. Fig. 4 of *Chen et al.* [2010] shows two distinct types of potentially unstable
 27 distributions. As a result of nightside injection, proton velocity distributions $f_p(\mathbf{v})$ near
 28 midnight are essentially bi-Maxwellian with $T_{\perp}/T_{\parallel} > 1$, where the subscripts indicate di-
 29 rections relative to the background magnetic field \mathbf{B}_0 . But between prenoon and duskside,
 30 energy-dependent ion injection leads to a velocity-ring-type distribution with a distinct
 31 $\partial f_p(v_{\perp})/\partial v_{\perp} > 0$ property.

32 Bi-Maxwellian $f_p(\mathbf{v})$ drive the Alfvén-cyclotron instability at frequencies $\omega_r < \Omega_p$ where
 33 Ω_p is the proton cyclotron frequency; there is an abundant literature on linear theory [e.g.,
 34 *Gendrin et al.*, 1984] and computer simulations [e.g., *Gary et al.*, 1995] of this instability
 35 and its associated enhanced fluctuations which many observers call "electromagnetic ion
 36 cyclotron (EMIC) waves" [e.g., *Anderson et al.*, 1992a, 1992b]. In contrast, the literature
 37 on the instabilities associated with proton velocity-ring-type distributions in the magne-
 38 tosphere is much less substantial; we here address the linear theory properties of such an
 39 instability.

40 Enhanced magnetic and electric field fluctuations at frequencies between the proton cy-
 41 clotron frequency and the lower hybrid frequency and at propagation nearly perpendicular

42 to \mathbf{B}_o are observed frequently near the equatorial plane of the terrestrial magnetosphere.
 43 Such enhanced fluctuations were first called “equatorial noise” [*Russell et al.*, 1970; *San-*
 44 *tolík et al.*, 2002, 2004], but more recently have been termed “magnetosonic waves”
 45 [*Perraut et al.*, 1982; *Horne et al.*, 2007; *Pokhotelov et al.*, 2008]. *Horne et al.* [2007]
 46 suggested that these enhanced fluctuations may accelerate electrons from tens of keV up
 47 to a few MeV in the outer radiation belt. This has stimulated substantial recent inter-
 48 est in these fluctuations [*Meredith et al.*, 2008, 2009; *Tao et al.*, 2009; *Shprits*, 2009; *Ni*
 49 *and Summers*, 2010; *Bortnik and Thorne*, 2010]. Magnetospheric observations character-
 50 ize the unstable proton velocity distributions $f_p(\mathbf{v})$ associated with these magnetosonic
 51 waves as having a velocity-ring type property or, more generally, with $\partial f_p(v_\perp)/\partial v_\perp > 0$
 52 where \perp denotes directions perpendicular to the background magnetic field \mathbf{B}_o [*Perraut*
 53 *et al.*, 1982; *Boardsen et al.*, 1992; *Meredith et al.*, 2008; *Denton et al.*, 2010].

54 If the positive slope of $f_p(v_\perp)$ is sufficiently large, linear kinetic dispersion theory in a
 55 relatively homogeneous, collisionless, magnetized plasma predicts that proton Bernstein
 56 modes at $0 < k_\parallel \ll k_\perp$ become unstable at real frequencies $\omega \simeq n\Omega_p$, where $n =$
 57 1, 2, 3 ... Electromagnetic linear theory of this instability has been addressed in the
 58 context of various space plasmas using the assumption of unmagnetized ions [*Akimoto et*
 59 *al.*, 1985] as well as the more complete model of magnetized ions [*Gul’elmi et al.*, 1975;
 60 *Perraut et al.*, 1982; *Boardsen et al.*, 1992; *Dendy and McClements*, 1993; *McClements*
 61 *and Dendy*, 1993; *McClements et al.*, 1994; *Horne et al.*, 2000; *Denton et al.*, 2010].
 62 Although some particle-in-cell simulations have addressed the nonlinear consequences of
 63 this instability in the electrostatic limit [e.g., *Lee and Birdsall*, 1979; *Roth and Hudson*,
 64 1985; *Janhunen et al.*, 2003; *Ashour-Abdalla et al.*, 2006], few simulations have addressed

65 the fully electromagnetic properties of this instability [*Lee and Birdsall, 1979*] in the high- β
66 regime appropriate for the terrestrial magnetosphere.

67 The term "magnetosonic waves" is a misnomer. In magnetohydrodynamic (MHD) the-
68 ory, magnetosonic waves correspond to the normal mode which, at propagation oblique
69 to the background magnetic field, is compressive and has a phase speed faster than the
70 incompressible Alfvén mode. Because MHD theory is limited to frequencies much below
71 the proton cyclotron frequency, the magnetosonic mode has historically been associated
72 with such very low frequencies. Unfortunately, many observers have chosen to apply the
73 "magnetosonic" label to their measurements of compressional modes at and above the
74 proton cyclotron frequency. We will bow to precedent and use this incorrect term in re-
75 ferring to observations of such fluctuations in the magnetosphere. But we insist on using
76 the more appropriate term "ion Bernstein mode instability" (often omitting "mode" for
77 the sake of brevity) in describing linear theory calculations of such growing and enhanced
78 fluctuations.

79 We denote the j th species plasma frequency as $\omega_j \equiv \sqrt{4\pi n_o e^2/m_j}$, the j th species cy-
80 clotron frequency as $\Omega_j \equiv e_j B_o/m_j c$, the j th component thermal speed as $v_j \equiv \sqrt{k_B T_j/m_j}$,
81 $\beta_j \equiv 8\pi n_j k_B T_j/B_o^2$, and $\tilde{\beta}_j \equiv 8\pi n_o k_B T_j/B_o^2$. The Alfvén speed is $v_A \equiv B_o/\sqrt{4\pi n_o m_i}$.
82 Here n_o is the total plasma density, \mathbf{B}_o denotes the uniform background magnetic field,
83 and we consider a two-species plasma of electrons (subscript e) and protons (subscript p).

84 The Cartesian coordinate system of our linear dispersion theory [*Gary, 1993*] admits
85 spatial variations in both the direction parallel to \mathbf{B}_o (denoted by \parallel) and one direction
86 perpendicular to the background field (denoted by \perp), but no spatial variations in the
87 other perpendicular direction (denoted by $\perp\perp$). So the real wavevector is defined as

88 $\mathbf{k} \equiv \hat{\mathbf{z}}k_{\parallel} + \hat{\mathbf{y}}k_{\perp} = \hat{\mathbf{z}}k \cos(\theta) + \hat{\mathbf{y}}k \sin(\theta)$ where θ denotes the wavevector direction relative
 89 to \mathbf{B}_o , and the complex frequency is $\omega = \omega_r + i\gamma$ where $\gamma > 0$ represents temporal growth
 90 of a normal mode of the plasma.

Here we consider the linear theory of the proton Bernstein mode instability driven by $\partial f_p(v_{\perp})/\partial v_{\perp} > 0$. We represent this nonthermal property of the proton velocity distribution via the difference of two isotropic Maxwellian distributions with different densities and temperatures [*Horne et al.*, 2000; *Denton et al.*, 2010]:

$$f_p(\mathbf{v}) = f_1(v) - f_2(v) \quad (1)$$

with

$$f_j(v) = \frac{n_j}{(2\pi v_j^2)^{3/2}} \exp(-v^2/2v_j^2)$$

91 Here $v^2 = v_{\parallel}^2 + v_{\perp}^2$, with $n_o = n_1 - n_2$ and $n_o T_p = n_1 T_1 - n_2 T_2$. The background electrons
 92 consist of a single component described by a Maxwellian velocity distribution.

From Table 6 of *Denton et al.* [2010], $n_o = 0.50 \text{ cm}^{-3}$, $k_B T_1 = 4.23 \text{ keV}$, and $B_o = 32.8 \text{ nT}$. Thus $v_A/c = 3.4 \times 10^{-3}$, $n_1/n_o = 6.3$, $n_2/n_o = 5.3$, $T_2/T_1 = 0.90$, and $T_e/T_1 = 0.10$. However, we choose $T_{\perp 1}/T_{\parallel 1} = T_{\perp 2}/T_{\parallel 2} = 1$, so that $T_p/T_1 = 1.53$, $\tilde{\beta}_1 = 0.80$ and $\tilde{\beta}_p = (T_p/T_1)\tilde{\beta}_1 = 1.224$. Using these parameters Figure 1 illustrates the reduced perpendicular velocity distribution

$$f_p(v_{\perp}) \equiv \int dv_{\parallel} d\phi f_p(\mathbf{v})$$

93 where ϕ is the azimuthal angle of the perpendicular component of the velocity. This shows
 94 the positive slope at relatively small v_{\perp} which is the free energy driving this instability.

2. Linear Theory

95 This section describes results obtained by numerically solving the electromagnetic linear
 96 kinetic dispersion equation for Maxwellian velocity distributions [*Gary, 1993*] without
 97 approximation. For the parameters stated in the Introduction, the maximum growth rate
 98 of the instability is $\gamma_m/\Omega_p \simeq 0.038$ at $k_m v_1/\Omega_p \simeq 3.10$, $\theta_m = 86.75^\circ$, and $\omega_r/\Omega_p \simeq 0.98$.
 99 The first three harmonics ($n = 2, 3$, and 4) of this mode are also unstable, although the
 100 maximum growth rates decrease monotonically with increasing n .

101 Figure 2 shows properties of the fundamental mode of the proton Bernstein instability
 102 as functions of wavenumber at θ_m , the angle of maximum growth rate. The magnetic
 103 fluctuations have both a transverse and a compressive component with $|\delta B_{\parallel}|^2 < |\delta B_{\perp\perp}|^2$
 104 at maximum growth rate. The corresponding electric field fluctuations are predominantly
 105 electrostatic, with $|\delta E_{\perp}|^2$ orders of magnitude larger than the other two electric field
 106 components. At maximum growth rate, the dimensionless ratio $|\delta \mathbf{E}|^2/|\delta \mathbf{B}|^2 \simeq 9.0 \times 10^{-5}$.

107 Figure 3 shows the same properties of the fundamental mode as functions of θ at k_m ,
 108 the wavenumber of maximum growth rate. For these parameters, the mode grows over a
 109 very limited range of less than two degrees in θ so, as in Figure 2, there is relatively little
 110 change in the dimensionless parameters over the range of propagation of the instability.
 111 This narrow range of unstable wavevectors implies that we can show the scaling properties
 112 of this instability by considering conditions at the maximum growth rate.

113 Figure 4 displays the wavenumber dependence of γ for the unstable regimes of the
 114 fundamental and the first three harmonics. The angles of propagation correspond to the
 115 relative maximum of the fundamental and the first three harmonics and are as labeled;
 116 the frequencies corresponding to the successive growth rate peaks are $\omega_r/\Omega_p = 0.978$,

117 1.970, 2.968, and 3.958. For these plasma parameters, the relative maximum growth rate
 118 diminishes with increasing harmonic number, as well as shifting to larger k_m and to more
 119 nearly perpendicular propagation. The phase speed at maximum growth rate is uniformly
 120 much less than v_A ; here $\omega_r/kv_A = 0.200, 0.226, 0.239,$ and 0.262 at the successive growth
 121 rate peaks. The phase speeds of the unstable modes are also considerably smaller than the
 122 proton thermal speed; here $\omega_r/kv_1 = 0.316, 0.357, 0.378, 0.414$ at the successive peaks of
 123 γ/Ω_p . These phase speeds of course correspond to the regime of strong positive derivative
 124 of $f_p(v_\perp)$, as indicated by the vertical arrows in Figure 1. The ratio of electric field energy
 125 to magnetic field energy density also increases monotonically with increasing frequency;
 126 $|\delta\mathbf{E}|^2/|\delta\mathbf{B}|^2 = 9.0 \times 10^{-5}, 2.8 \times 10^{-4}, 5.8 \times 10^{-4},$ and 8.8×10^{-4} at the successive growth
 127 rate peaks.

128 So far we have plotted the instability growth rate as a function of a single parameter;
 129 for example, in Figure 2 θ is fixed and γ/Ω_p is plotted as a function of wavenumber. This
 130 plot suggests that significant instability growth is limited to a relatively narrow band
 131 of wavenumbers. Figure 5a provides a different perspective, showing the growth rate of
 132 the fundamental as a two-dimensional function of k_\perp and θ . This figure shows that the
 133 apparent narrow slice of instability growth actually extends over a much broader range
 134 of wavenumber values; similarly the θ range which corresponds to appreciable growth is
 135 considerably broader than that indicated in Figure 3. Figure 5b shows a similar plot of
 136 $\gamma(k_\perp, \theta)/\Omega_p$ for the unstable part of the first harmonic, again implying a much broader
 137 range of unstable wavenumbers and quasi-perpendicular propagation angles than would
 138 be suggested by one-dimensional cuts through this plot.

139 Figure 6 illustrates linear properties at maximum growth rate of the fundamental of
 140 this instability as a function of $\tilde{\beta}_1$ under the condition that all other dimensionless pa-
 141 rameters stated in the Introduction are held constant. An interesting feature of panel (a)
 142 is that γ_m/Ω_p is not a monotonic function of the proton β , but, as in Table 7 of *Denton*
 143 *et al.* [2010], has a relative maximum near $\tilde{\beta}_1 \simeq 0.30$, that is, $\tilde{\beta}_p \simeq 0.46$. In panel (b)
 144 $k_m v_1/\Omega_e$ shows much less variation with $\tilde{\beta}_p$ than does $k_m c/\omega_p$, suggesting that the pro-
 145 ton thermal gyroradius, rather than the proton inertial length, is the more appropriate
 146 factor to describe the scaling of wavenumber of maximum growth. Figure 6(c) shows
 147 that increasing proton β implies that the direction of propagation of the instability moves
 148 monotonically away from the perpendicular. And Figure 6(d) shows that the magnetic
 149 compressibility, i.e., $C_{\parallel} \equiv |\delta B_{\parallel}|^2/|\delta \mathbf{B}|^2$, increases with increasing proton β [*Denton et al.*,
 150 2010], consistent with the expectation that electrostatic instabilities should become more
 151 strongly electromagnetic as this parameter increases. Thus Figure 6 implies there are
 152 three distinct regimes for this instability: relatively weak growth in the electrostatic limit
 153 of proton $\beta = 0$, relatively strong growth with electromagnetic properties at intermediate
 154 proton β , and then growth rate diminishing to zero at relatively large proton β .

155 Figure 7 shows the maximum growth rate of the instability fundamental as a function
 156 of T_e/T_1 . The γ_m/Ω_p is a strongly decreasing function of the electron-proton temperature
 157 ratio. Sample computations not shown here show that the three unstable harmonics also
 158 have their growth rates reduced to damping for sufficiently large T_e/T_1 . This indicates
 159 that this instability is subject to strong electron Landau damping as the relative electron
 160 temperature increases. This, in turn, suggests that hybrid simulations, in which electrons
 161 are represented as a fluid, do not provide a full description of the physics of this instability,

162 and that particle-in-cell simulations are a more appropriate tool to simulate the nonlinear
 163 physics of this growing mode.

164 If we increase the free energy associated $\partial f_p(v_\perp)/\partial v_\perp > 0$, we expect that the maximum
 165 instability growth rate should increase. If, given the constraint $n_1/n_o - n_2/n_o = 1.0$, we
 166 increase n_1/n_o and hold all other dimensionless plasma parameters constant, we dig a
 167 deeper hole in the $v_\perp \simeq 0$ part of the proton velocity distribution; the corresponding
 168 increase in the proton free energy yields an increase in instability growth rate.

169 Figure 8 illustrates this; here the dimensionless plasma parameters are the same as
 170 those used in Figure 4 except that $n_1/n_o = 6.8$ and $n_2/n_o = 5.8$. This figure shows
 171 that this increase in the proton free energy leads not only to an increase in γ_m/Ω_p for the
 172 fundamental mode, but also to a shift in the maximum γ_m/Ω_p to the first harmonic mode,
 173 and an expansion of unstable harmonics out to $n = 8$. Figure 8 demonstrates that, as the
 174 proton free energy is increased, the overall maximum growth rate moves to higher proton
 175 cyclotron harmonics, with $\omega_r/\Omega_p \gg 1$ as in the extreme cases illustrated in *Gul'elmi et*
 176 *al.* [1975], *Dendy and McClements* [1993], and *Horne et al.* [2000]. Comparison against
 177 Figure 4 shows, however, that the increase in free energy and maximum growth rate
 178 does not significantly change the range of phase speeds at the growth rate peaks of the
 179 fundamental and harmonics; for Figure 8 this range is $0.336 \leq \omega_r/kv_1 \leq 0.418$.

180 Our linear code directly yields the following additional results not illustrated here.
 181 Adding a small component of cold protons reduces the maximum growth rate of the
 182 instability. Making both f_1 and f_2 anisotropic in the sense of $T_{\perp j}/T_{\parallel j} > 1$ reduces the
 183 maximum growth rate, whereas the opposite sense of the anisotropy acts to enhance
 184 γ_m/Ω_p of the proton Bernstein instability. This latter result can be understood as follows:

185 If the instability growth rate is driven by the proton term proportional to $\partial f_p(v_\perp)/\partial v_\perp$,
 186 and if $f_p(\mathbf{v})$ is given by Equation (1), then the v_\perp derivative yields factors of $1/T_{\perp j}$ for
 187 $j = 1$ and 2 . So if the $T_{\parallel j}$ are fixed, increasing the $T_{\perp j}$ is likely to reduce γ_m/Ω_p .

3. Conclusions

188 We have carried out numerical solutions of the full linear kinetic dispersion equation
 189 for the proton Bernstein instability driven by a proton velocity distribution $f_p(\mathbf{v})$ such
 190 that $\partial f_p(v_\perp)/\partial v_\perp > 0$ at relatively small v_\perp . Our results are consistent with previous
 191 theoretical results; the instability propagates almost perpendicular to \mathbf{B}_o with relative
 192 maxima not only near $\omega_r \simeq \Omega_p$, but also at successive harmonics of the proton cyclotron
 193 frequency. For plasma parameters similar to those reported by *Denton et al.* [2010], we
 194 find that the $\omega_r \simeq \Omega_p$ fundamental has the largest growth rate, but that higher order
 195 harmonics may also be unstable for sufficiently large free energy in the proton velocity
 196 distribution. The maximum instability growth rate is a monotonically decreasing function
 197 of the electron-to-proton temperature ratio, but has its largest value at an intermediate
 198 value of the proton β (~ 0.5 for the parameters considered here).

199 We have followed *Denton et al.* [2010] in using the subtracted Maxwellian proton
 200 velocity distribution of Equation (1) because we, like *Denton et al.*, have access to a
 201 linear kinetic theory code based upon Maxwellian velocity distributions [*Gary*, 1993].
 202 However, our maximum growth rates (like those of *Denton et al.*) are relatively weak; for
 203 comparison, *Akimoto et al.* [1985] use a cold ion velocity ring in their dispersion equation
 204 and obtain much stronger instability growth with $\gamma_m > \Omega_p$. Furthermore, sample particle-
 205 in-cell simulations using a subtracted Maxwellian proton distribution yield similarly weak
 206 growth and relatively low saturation values of the fluctuating fields [*Liu et al.*, 2010].

207 However, magnetospheric observations demonstrate that that proton velocity distribu-
208 tions associated with the so-called “magnetosonic waves” may display much more free
209 energy than can be conveniently represented in the subtracted Maxwellian model [e.g.,
210 *Perraut et al.*, 1982; *Boardsen et al.*, 1992; *Meredith et al.*, 2008; *Denton et al.*, 2010].
211 So the primary goal of the research described here has not been to reproduce specific
212 magnetospheric observations, but rather to demonstrate general scaling properties of the
213 proton Bernstein instability, for guiding further observational and computational studies
214 of the enhanced fluctuations which arise from this growing mode.

215 **Acknowledgments.** This work was performed under the auspices of the U.S. Depart-
216 ment of Energy (DOE). It was supported primarily by the Defense Threat Reduction
217 agency under the “Basic Research for Combating Weapons of Mass Destruction (WMD)”
218 Program, project IACRO 07-4323I. Work at Dartmouth College was supported by NSF
219 grants ANT-0538379 and ATM-0120950 (Center for Integrated Space Weather Modeling,
220 CISM, funded by the NSF Science and Technology Centers Program).

References

- 221 Akimoto, K., K. Papadopoulos, and D. Winske (1985), Lower-hybrid instabilities driven
222 by an ion velocity ring, *J. Plasma Phys.*, *34*, 445.
- 223 Anderson, B. J., R. E. Erlandson, and L. J. Zanetti (1992a), A statistical study of Pc 1-2
224 magnetic pulsations in the equatorial magnetosphere, 1. Equatorial occurrence distri-
225 butions, *J. Geophys. Res.*, *97*, 3075.
- 226 Anderson, B. J., R. E. Erlandson, and L. J. Zanetti (1992b), A statistical study of Pc 1-2
227 magnetic pulsations in the equatorial magnetosphere, 2. Wave properties, *J. Geophys.*

- 228 *Res.*, *97*, 3089.
- 229 Ashour-Abdalla, M., J. N. Leboeuf, D. Schriver, J.-M. Bosqued, N. Cornilleau-Wehrin,
230 V. Sotnikov, A. Marcaudon, and A. N. Fazakerley (2006), Instabilities driven by ion
231 shell distributions observed by Cluster in the midaltitude plasma sheet boundary layer,
232 *J. Geophys. Res.*, *111*, A10223.
- 233 Boardsen, S. A., D. L. Gallagher, D. A. Gurnett, W. K. Peterson, and J. L. Green (1992),
234 Funnel-shaped, low-frequency equatorial waves, *J. Geophys. Res.*, *97*, 14,967.
- 235 Bortnik, J., and R. M. Thorne (2010), Transit time scattering of energetic electrons due
236 to equatorially confined magnetosonic waves, *J. Geophys. Res.*, *115*, A07213.
- 237 Chen, L., R. M. Thorne, V. K. Jordanova, C.-P. Wang, M. Gkioulidou, L. Lyons, and R.
238 B. Horne (2010), Global simulation of EMIC wave excitation during the 21 April 2001
239 storm from coupled RCM-RAM-HOTRAY modeling, *J. Geophys. Res.*, *115*, A07209.
- 240 Dendy, R. O., and K. G. McClements (1993), Ion cyclotron wave emission at the quasi-
241 perpendicular bow shock, *J. Geophys. Res.*, *98*, 15,531.
- 242 Denton, R. E., M. J. Engebretson, A. Keiling, A. P. Walsh, S. P. Gary, P. M. E. Décréau,
243 C. A. Cattell, and H. Réme (2010), Multiple harmonic ULF waves in the plasma sheet
244 boundary layer: Instability analysis, *J. Geophys. Res.*, submitted.
- 245 Gary, S. P. (1993), *Theory of Space Plasma Instabilities*, Cambridge University Press.
- 246 Gary, S. P., M. F. Thomsen, L. Yin, and D. Winske (1995), Electromagnetic proton
247 cyclotron instability: Interactions with magnetospheric protons, *J. Geophys. Res.*, *100*,
248 21,961.
- 249 Gendrin, R., M. Ashour-Abdalla, Y. Omura, and K. Quest (1984), Linear analysis of ion
250 cyclotron interaction in a multicomponent plasma, *J. Geophys. Res.*, *89*, 9119.

- 251 Gul’elmi, A. V., B. I. Klaine, and A. S. Potapov (1975), Excitation of magnetosonic waves
252 with discrete spectrum in the equatorial vicinity of the plasmopause, *Planet. Space Sci.*,
253 *23*, 279.
- 254 Horne, R. B., G. V. Wheeler, and H. St. C. K. Alleyne (2000), Proton and electron heating
255 by radially propagating fast magnetosonic waves, *J. Geophys. Res.*, *105*, 27,597.
- 256 Horne, R. B., R. M. Thorne, S. A. Glauert, N. P. Meredith, D. Pokhotelov, and O. Santolík
257 (2007), Electron acceleration in the Van Allen radiation belts by fast magnetosonic
258 waves, *Geophys. Res. Lett.*, *34*, L17107.
- 259 Janhunen, P., A. Olsson, A. Vaivads, and W. K. Peterson (2003), Generation of Bernstein
260 waves by ion shell distributions in the auroral region, *Ann. Geophys.*, *21*, 881.
- 261 Jordanova, V. K., J. U. Kozyra, A. F. Nagy, and G. V. Khazanov (1997), Kinetic model
262 of the ring current-atmosphere interactions, *J. Geophys. Res.*, *102*, 14,279.
- 263 Lee, J. K., and C. K. Birdsall (1979), Velocity space ring-plasma instability, magnetized,
264 Part II: Simulation, *Phys. Fluids*, *22*, 1315.
- 265 Liu, K., S. P. Gary, and D. Winske (2010), Excitation of Bernstein waves in the terrestrial
266 magnetosphere: Particle-in-cell simulations, *Geophys. Res. Lett.*, submitted.
- 267 McClements, K. G., and R. O. Dendy (1993), Ion cyclotron harmonic wave generation by
268 ring protons in space plasmas, *J. Geophys. Res.*, *98*, 11,689.
- 269 McClements, K. G., R. O. Dendy, and C. N. Lashmore-Davies (1994), A model for the
270 generation of obliquely propagating ULF waves near the magnetic equator, *J. Geophys.*
271 *Res.*, *99*, 23,685.
- 272 Meredith, N. P., R. B. Horne, and R. R. Anderson (2008), Survey of magnetosonic waves
273 and proton ring distributions in the Earth’s inner magnetosphere, *J. Geophys. Res.*,

274 113, A06213.

275 Meredith, N. P., R. B. Horne, S. A. Glauert, D. N. Baker, S. G. Kanekal, and J. M. Albert
276 (2009), Relativistic electron loss timescales in the slot region, *J. Geophys. Res.*, 114,
277 A03222.

278 Ni, B., and D. Summers (2010), Resonance zones for electron interaction with plasma
279 waves in the Earth's dipole magnetosphere. II. Evaluation for oblique chorus, hiss, elec-
280 tromagnetic ion cyclotron waves, and magnetosonic waves, *Phys. Plasmas*, 17, 042903.

281 Perraut, S., A. Roux, P. Robert, R. Gendrin, J.-A. Sauvaud, J.-M. Bosqued, G. Kremser,
282 and A. Korth (1982), A systematic study of ULF waves above F_{H+} from GEOS 1 and 2
283 measurements and their relationships with proton ring distributions, *J. Geophys. Res.*,
284 87, 6219.

285 Pokhotelov, D., F. Feveuvre, R. B. Horne, and N. Cornilleau-Wehrin (2008), Survey of
286 ELF-VLF plasma waves in outer radiation belt observed by Cluster STAFF-SA exper-
287 iment, *Ann. Geophys.*, 26, 3269.

288 Roth, I., and M. K. Hudson (1985), Lower hybrid heating of ionospheric ions due to ion
289 ring distributions in the cusp, *J. Geophys. Res.*, 90, 4191.

290 Russell, C. T., R. E. Holzer, and E. J. Smith (1970), OGO 3 observations of ELF noise
291 in the magnetosphere 2. The nature of equatorial noise, *J. Geophys. Res.*, 75, 755.

292 Santolík, O., J. S. Pickett, D. A. Gurnett, M. Maksimovic, and N. Cornilleau-Wehrin
293 (2002), Spatiotemporal variability and propagation of equatorial noise observed by Clus-
294 ter, *J. Geophys. Res.*, 107, 1495.

295 Santolík, O., F. Nemeč, K. Cereová, E. Macúsova, Y. de Conchy, and N. Cornilleau-
296 Wehrin (2004), Systematic analysis of equatorial noise below the lower hybrid fre-

297 quency, *Ann. Geophys.*, *22*, 2587.

298 Shprits, Y. Y. (2009), Potential waves for pitch-angle scattering of near-equatorially mir-
299 roring energetic electrons due to the violation of the second adiabatic invariant, *Geophys.*
300 *Res. Lett.*, *36*, L12106.

301 Tao, X., J. M. Albert, and A. A. Chan (2009), Numerical modeling of multidimensional
302 diffusion in the radiation belts using layer methods, *J. Geophys. Res.*, *114*, A02215.

303 Winske, D., and N. Omidi (1993), Hybrid codes: Methods and applications, in Computer
304 Space Plasma Physics: Simulation Techniques and Software, Edited by H. Matsumoto
305 and Y. Omura, p. 103, Terra Scientific Publishers, Tokyo.

306 Winske, D., and K. B. Quest (1988), Magnetic field and density fluctuations at perpen-
307 dicular supercritical collisionless shocks, *J. Geophys. Res.*, *93*, 9681.

308 Winske, D., L. Yin, N. Omidi, H. Karimabadi and K. B. Quest (2003), Hybrid codes:
309 Past, Present and Future, in Space Plasma Simulation, edited by J. Buechner, C. T.
310 Dum and M. Scholer, Springer Verlag, pp. 140-169.

Figure 1. The solid line indicates the reduced proton perpendicular velocity distribution (in arbitrary units) in the subtracted Maxwellian model using the dimensionless plasma parameters stated in the Introduction. The dashed line indicates a reduced Maxwellian distribution with density n_o and temperature T_1 . The two vertical arrows indicate the phase speeds ω_r/kv_1 at relative maximum growth rates of the fundamental ($n = 1$) and third harmonic ($n = 4$) modes.

Figure 2. Linear theory properties of the fundamental proton Bernstein instability as functions of the wavenumber at $\theta_m = 86.75^\circ$. (a) Real frequency (solid line) and growth rate (dotted line). (b) Energy density of fluctuating magnetic field components as labeled. (c) Energy density of fluctuating electric field components as labeled. Here and in all subsequent figures the dimensionless plasma parameters are as given in the Introduction, unless stated otherwise.

Figure 3. Linear theory properties of the fundamental proton Bernstein instability as functions of the propagation angle at $k_m v_1 / \Omega_p = 3.10$. (a) Real frequency (solid line) and growth rate (dotted line). (b) Energy density of fluctuating magnetic field components as labeled. (c) Energy density of fluctuating electric field components as labeled.

Figure 4. Linear theory growth rates of the fundamental and first three harmonics of the proton Bernstein instability as functions of wavenumber. The angles of propagation correspond to the relative maxima of each mode and are as labeled.

Figure 5. Linear theory growth rates as a function of perpendicular wavenumber and propagation angle for the proton Bernstein instability. The left-hand panel (a) illustrates γ/Ω_p of the fundamental with $\omega_r/\Omega_p \simeq 1.0$, whereas the right-hand panel (b) shows γ/Ω_p of the first harmonic with $\omega_r/\Omega_p \simeq 2.0$. The asterisk in panel (a) marks the maximum growth rate $\gamma_m/\Omega_p = 0.038$ at $kv_1/\Omega_p = 3.10$ and $\theta = 86.75^\circ$. The asterisk in panel (b) indicates the maximum growth rate of the first harmonic with $\gamma_m/\Omega_p = 0.036$ at $kv_1/\Omega_p = 5.52$ and $\theta = 87.90^\circ$. The solid lines indicate the contours of $\gamma/\Omega_p = 0.03$.

Figure 6. Linear theory properties of the fundamental proton Bernstein instability at maximum growth rate as functions of $\tilde{\beta}_1$. (a) Maximum growth rate, (b) wavenumber at maximum growth rate, (c) propagation angle at maximum growth rate, and (d) magnetic compressibility $C_{\parallel} \equiv |\delta B_{\parallel}|^2/|\delta \mathbf{B}|^2$.

Figure 7. Linear theory of the fundamental proton Bernstein instability: maximum growth rate as a function of T_e/T_1 .

Figure 8. Linear theory growth rates of the fundamental and first seven harmonics of the proton Bernstein instability as functions of wavenumber for $n_1/n_o = 6.8$ and $n_2/n_o = 5.8$. The angles of propagation for the modes shown here are $\theta = 86.35^\circ, 87.65^\circ, 88.30^\circ, 88.60^\circ, 88.90^\circ, 89.00^\circ, 89.10^\circ$, and 89.15° for the fundamental and successive harmonics.

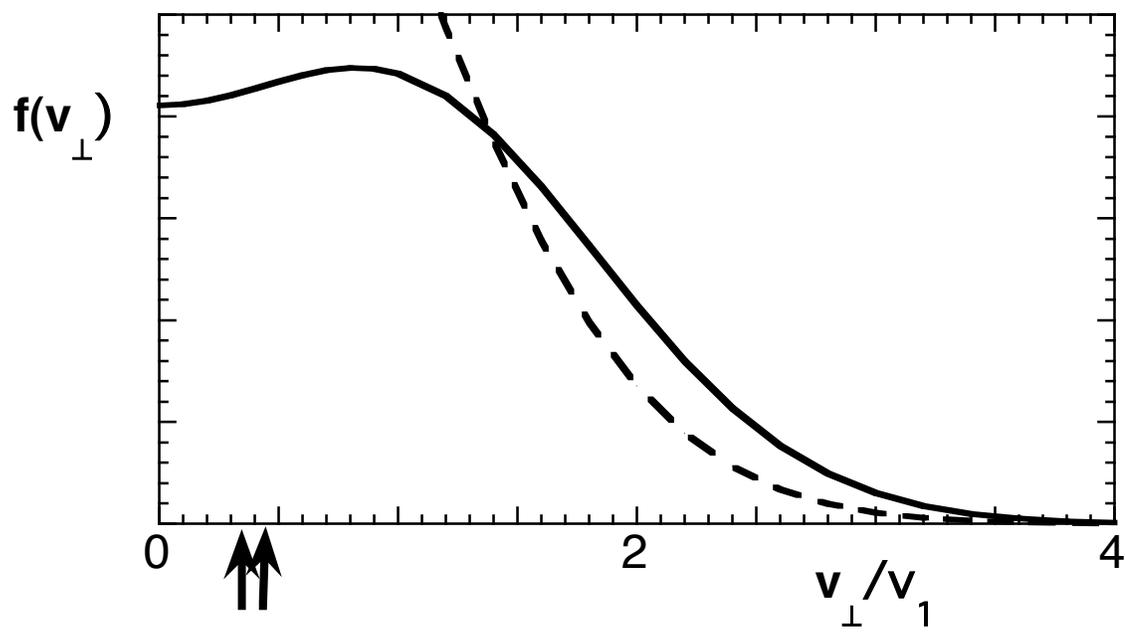


Figure 1

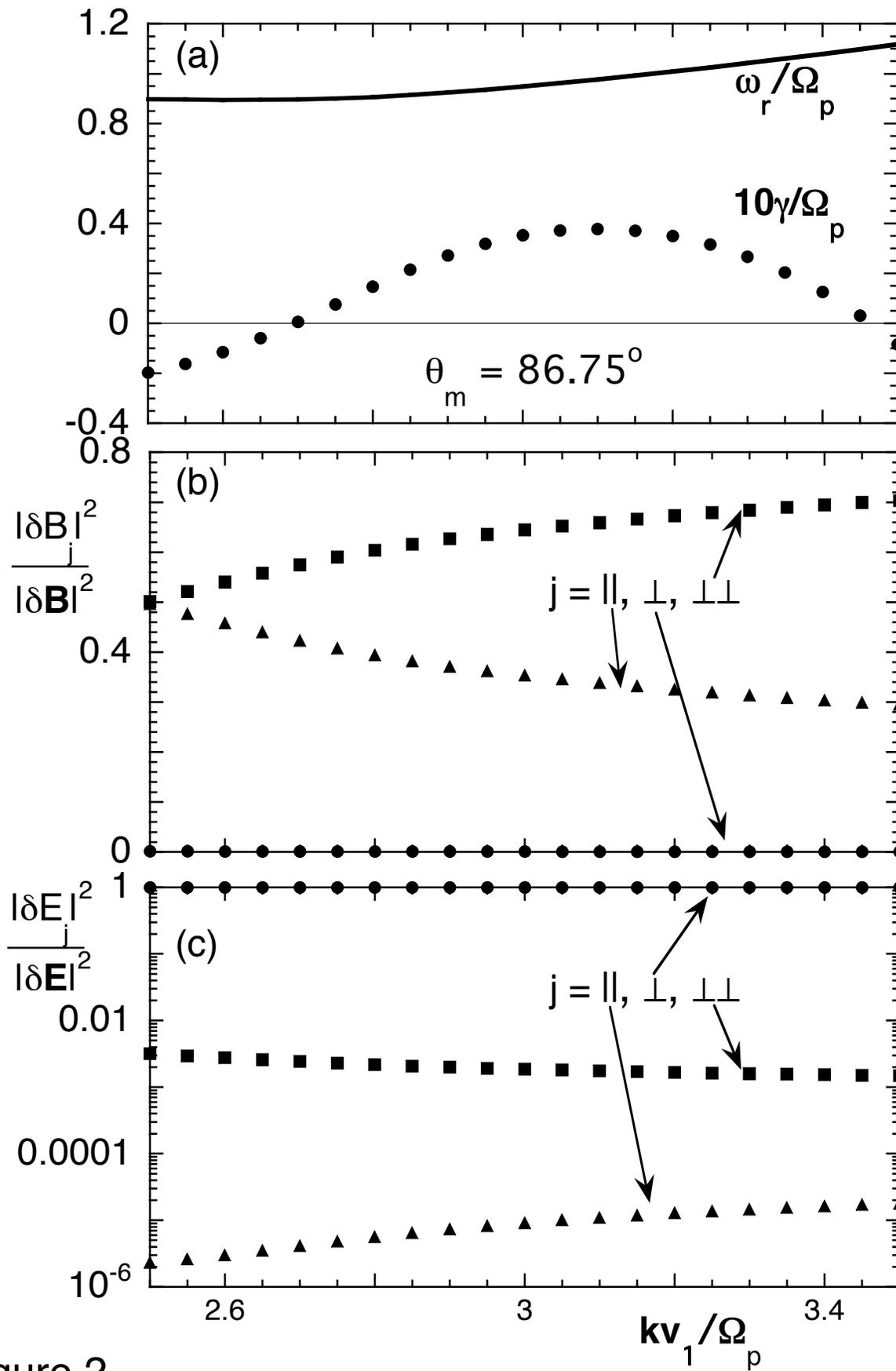


Figure 2

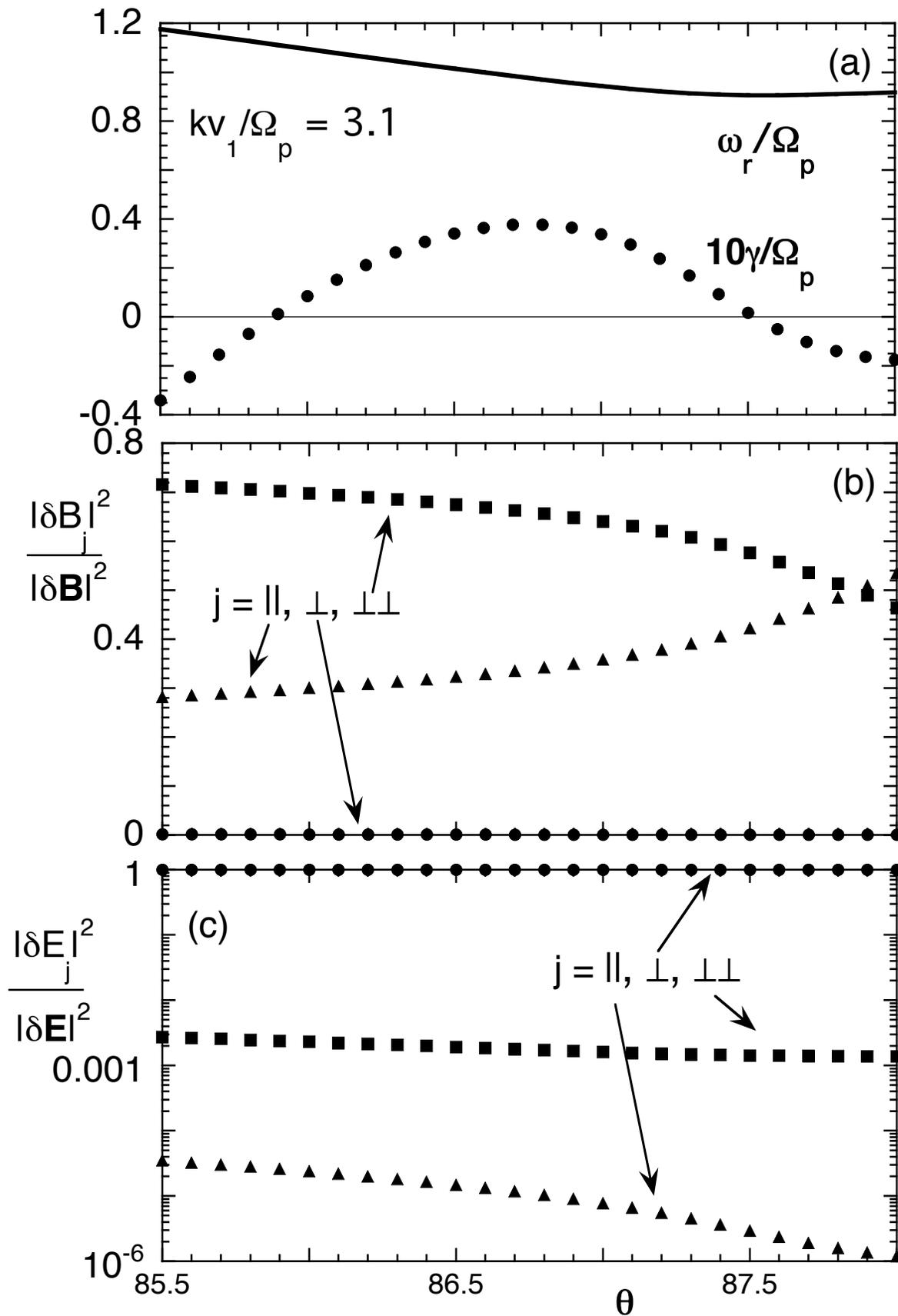


Figure 3

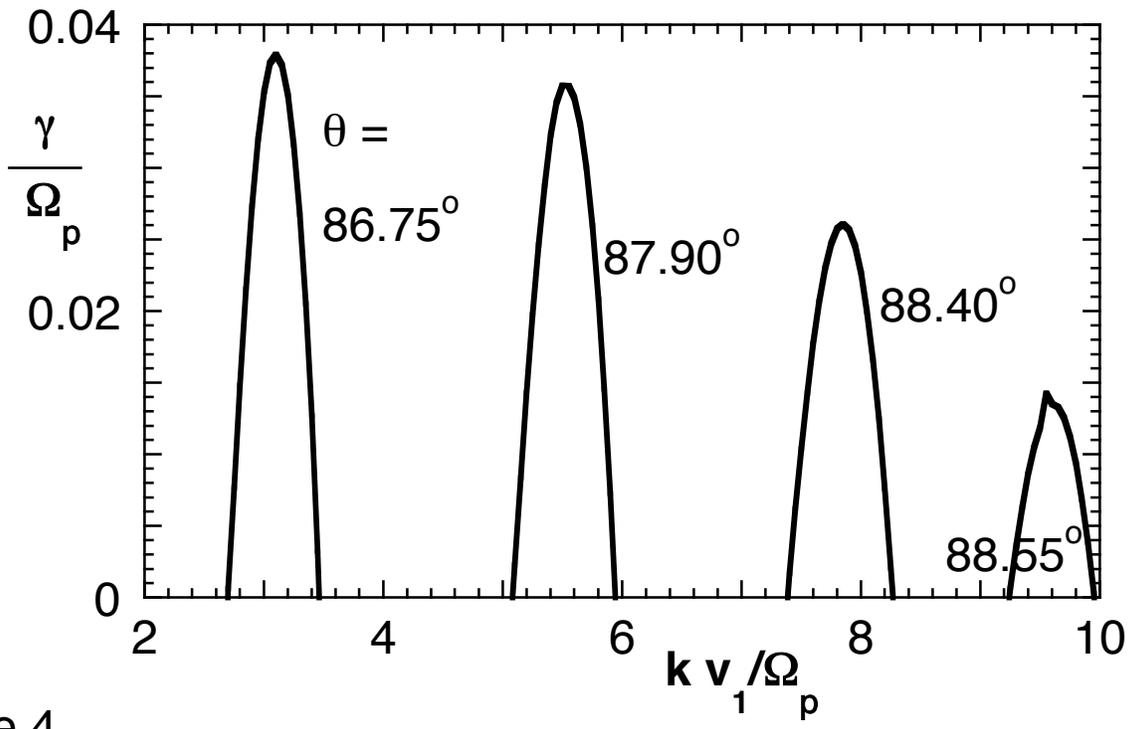
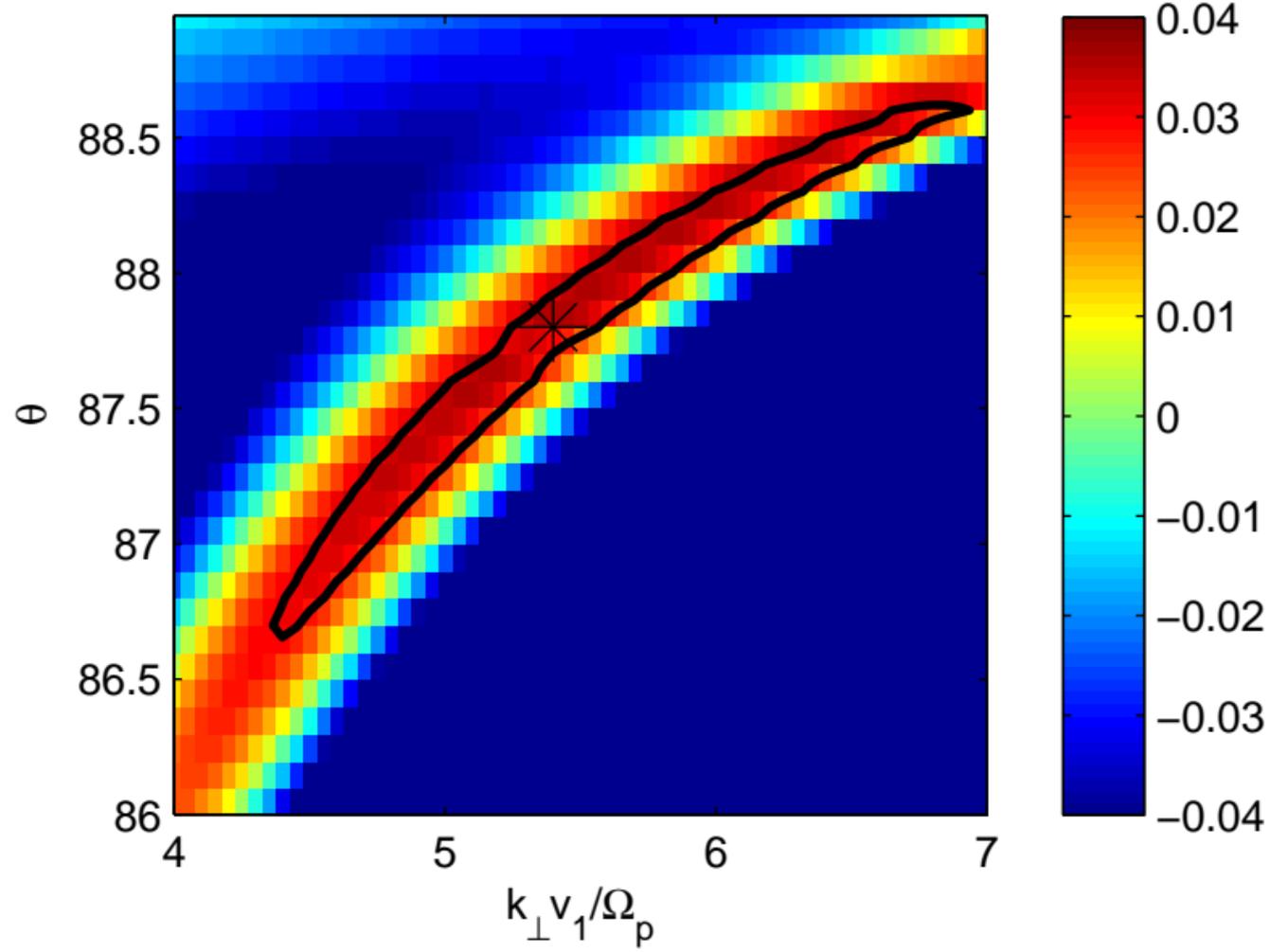
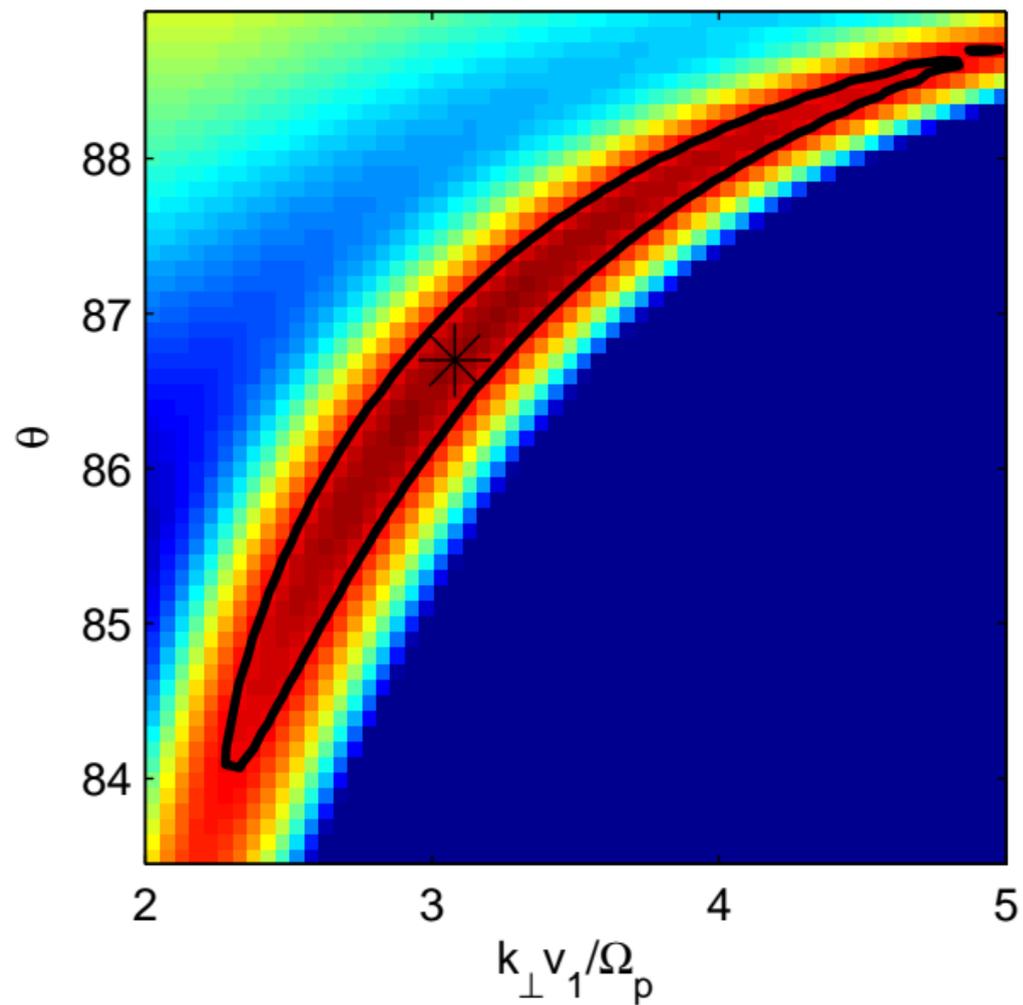


Figure 4



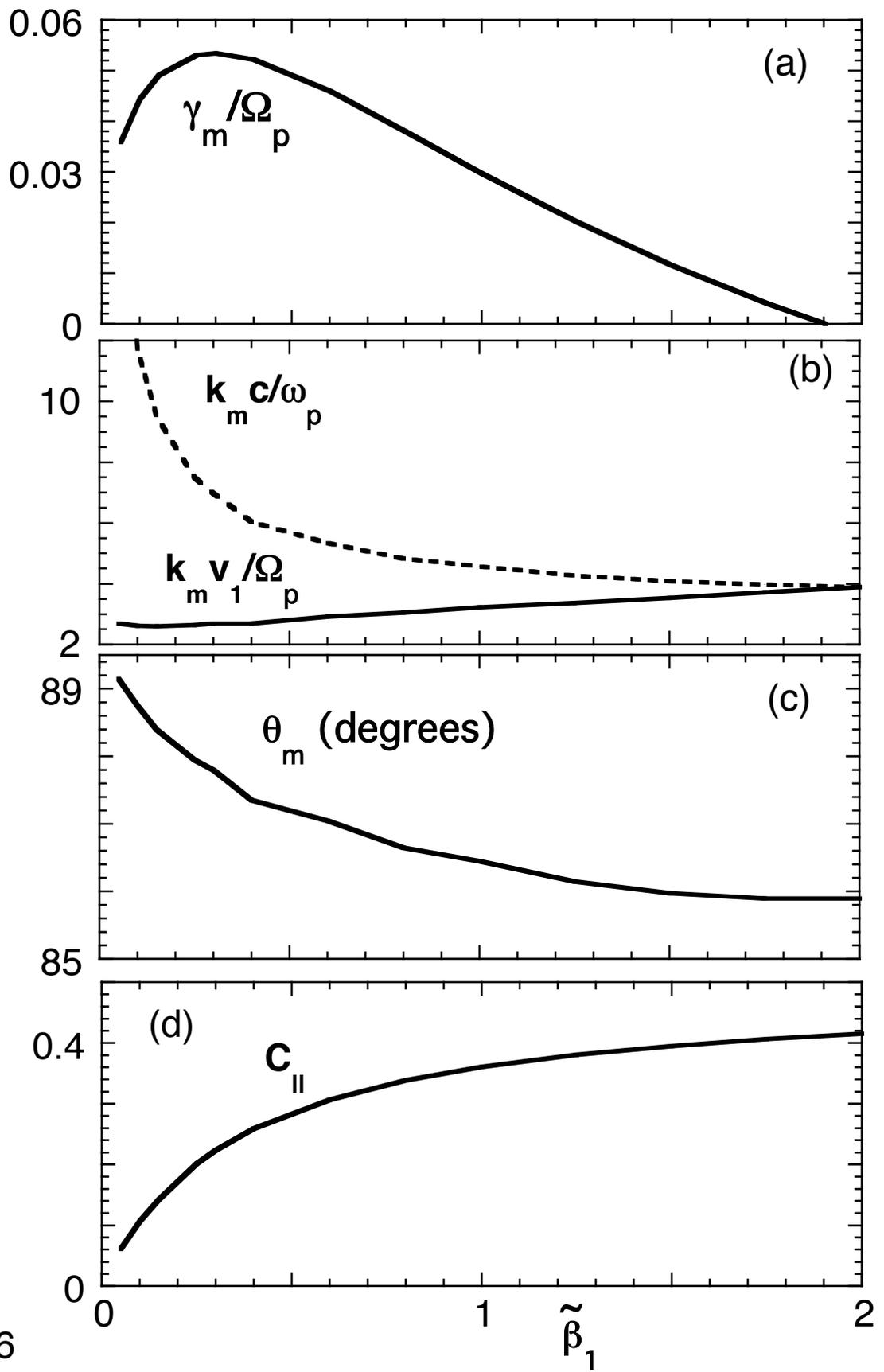


Figure 6

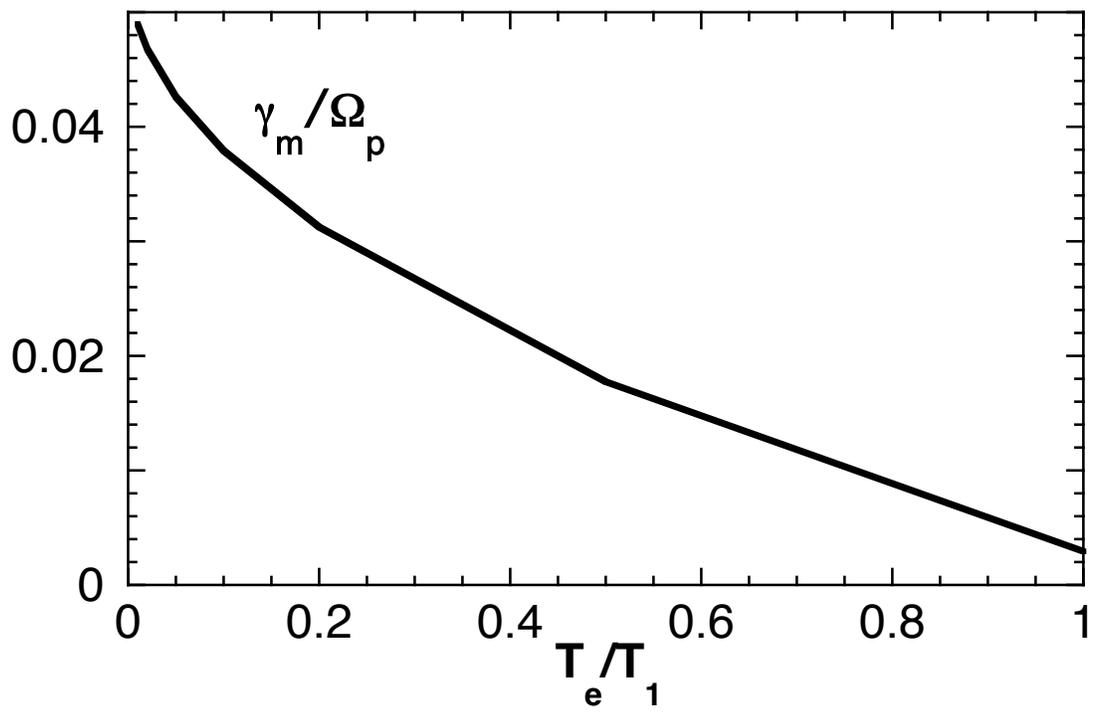


Figure 7

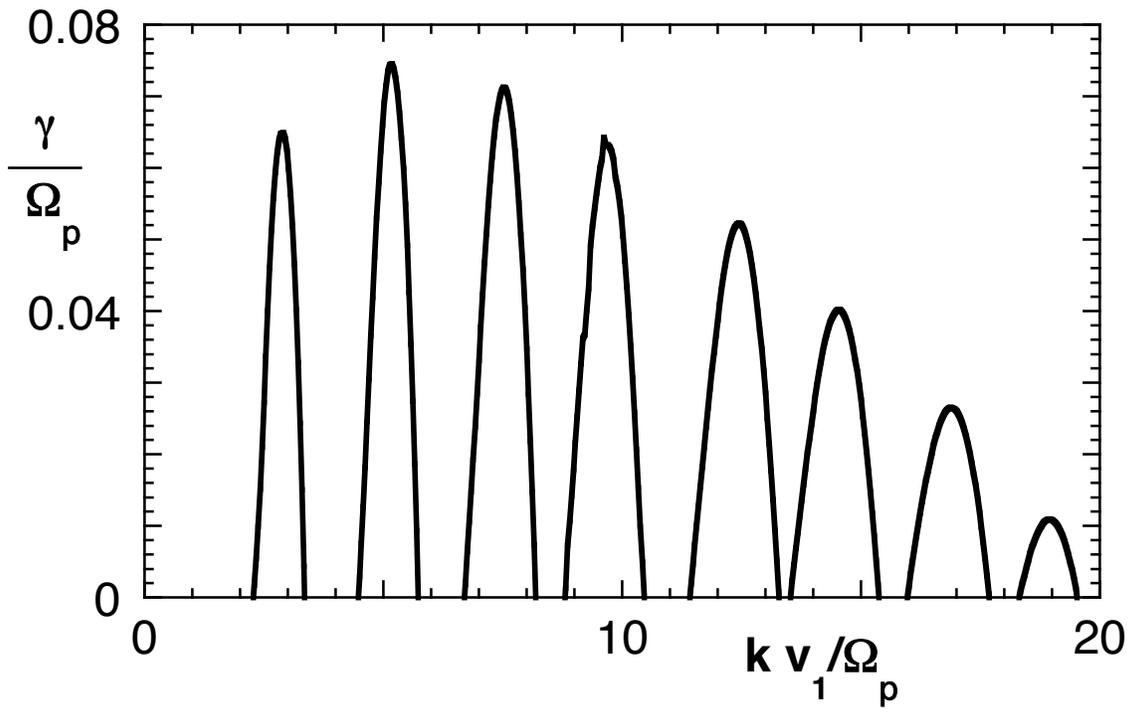


Figure 8